Received: 25 November 2024 | Revised: 1 April 2025 | Accepted: 8 April 2025

DOI: 10.1002/inf2.70034

WILEY

RESEARCH ARTICLE

Water- and oxidation-resistant MXenes for advanced electromagnetic interference shielding applications

Young Ho Jin[1] | Ju-Hyoung Han[1] | Jaeeun Park[1] | Mincheal Kim[2] | Shi-Hyun Seok[1] | Yujin Chae[1] | Yeoseon Sim[1] | Sangjin Seo[3] | Hyeonwoo Lee[1] | Jaewon Wang[1] | Jihoon Yang[1] | Sora Jang[1] | Juwon Han[1] | Haeng Un Yeo[1] | Sung Hyun Park[4] | EunMi Choi[2] | Taesung Kim[3] | Soon-Yong Kwon[1]

[1]Department of Materials Science and Engineering and Graduate School of Semiconductor Materials and Devices Engineering, Ulsan National Institute of Science and Technology (UNIST), Ulsan, Republic of Korea

[2]Department of Electrical Engineering, Ulsan National Institute of Science and Technology (UNIST), Ulsan, Republic of Korea

[3]Department of Mechanical Engineering, Ulsan National Institute of Science and Technology (UNIST), Ulsan, Republic of Korea

[4]Clean Energy Transition Group, Korea Institute of Industrial Technology (KITECH), Jeju, Republic of Korea

Correspondence
Soon-Yong Kwon, Department of Materials Science and Engineering and Graduate School of Semiconductor Materials and Devices Engineering, Ulsan National Institute of Science and Technology (UNIST), Ulsan 44919, Republic of Korea.
Email: sykwon@unist.ac.kr

Funding information
National Research Foundation (NRF) of Korea, Grant/Award Numbers: RS-2024-00408180, RS-2024-00344270; Korea Institute of Energy Technology Evaluation and Planning (KETEP), Grant/Award Number: RS-2024-00398425

Abstract

Two-dimensional transition metal carbides and nitrides (MXenes) show great promise for electromagnetic interference (EMI) shielding. However, their susceptibility to oxidation, particularly in humid environments or water, limits their industrial applications. This study introduces a straightforward method for developing functionalized MXenes (F-MXenes) with significantly enhanced oxidation resistance and environmental stability, which are critical factors for industrial scalability. The resulting F-MXenes disperse easily in non-polar solvents, adhere well to various substrates, and remain highly stable under harsh conditions in an accelerated oxidation test at 100°C and 80% relative humidity for 49 days; F-MXenes retained 93% of their initial electrical resistance. Additionally, these films withstand water exposure, maintain superior current retention in seawater and corrosive environments, and exhibit high flexibility (10 000 bending cycles) and tensile strength (35 MPa). Notably, the EMI shielding effectiveness of the hydrophobic F-MXene films, produced using scalable techniques such as spray and blade coating, far exceeds that of previously reported hydrophobic MXene films and MXene composites, achieving 52–77 dB at thicknesses of 5–40 μm. This study highlights the potential of F-MXene as high-performance, scalable EMI-shielding coatings, particularly in humid or water-exposed environments.

KEYWORDS

electromagnetic interference (EMI) shielding, environmental stability, hydrophobic MXenes, oxidation resistance, scalable coating

1 | INTRODUCTION

As a novel class of two-dimensional (2D) materials with unique structural, electrical, and electrochemical properties, transition metal carbides and nitrides (MXenes) have been extensively studied.[1–5] MXenes exhibit high electromagnetic interference (EMI) shielding effectiveness (SE), reaching up to 93 dB at a thickness of 40 μm,[6] due to their layered structure (enabling multiple reflection and absorption of EM waves),[7] high electrical conductivity (up to 20 000 S cm^{-1}),[8] and large surface area which facilitates thin-film fabrication.[9] These properties make MXenes ideal for high-performance EMI shielding.[6,10,11] Additionally, they can be processed using scalable solution-based techniques, such as spray and blade coating, making them suitable for industrial-scale production.[12–14] Their flexibility and mechanical strength further enhance their applicability in shielding materials that conform to various shapes and structures.[4,15,16]

However, MXenes are highly susceptible to oxidation, which significantly degrades their electrical conductivity and flexibility—critical properties for their practical use.[17–20] Current strategies to mitigate oxidation include thermal treatment (with or without additives),[21–23] surface passivation with alkali ions,[24,25] and composite formation with hydrophobic polymers.[26–29] Thermal treatment, often performed after film fabrication, typically requires high temperatures in an inert or hydrogen atmosphere. Low-temperature processes necessitate additives, which can be resource intensive and challenging for large-scale applications. Surface passivation with alkali ions can cause crumpling of MXenes, reducing dispersion stability and requiring additional purification steps. In hydrophobic polymer composites, MXenes typically serve as fillers in a multilayered structure, which limits their full potential.

A promising alternative for preventing oxidation is dispersing MXenes in non-polar solvents, shielding them from oxygen and water, and extending their shelf life for industrial applications.[30,31] Surface modification with organic molecules imparts hydrophobicity by forming physical or chemical bonds with MXene surface functional groups.[32–36] However, this method often requires harsh processing conditions to establish stable bonds and increases the interlayer spacing due to long alkyl chains, leading to oxidation and a significant drop in electrical conductivity. Moreover, most studies have focused on preparing nonpolar dispersions, with limited exploration of their large-scale integration into EMI shielding films. Therefore, developing an efficient, scalable, and environmentally stable approach to enhance the oxidation and water resistance of MXenes while preserving their electrical conductivity and enabling industrial-scale integration is crucial for advancing their practical applications.

In this study, we developed a scalable and environmentally stable functionalized MXene (F-MXene) by attaching alkyl amines of varying chain lengths (e.g., dodecyl-, tetradecyl-, and hexadecyl-amine) to the MXene surface. The resulting F-MXenes readily disperse in nonpolar solvents such as toluene, chlorobenzene, and heptane and can be coated onto various substrates including glass, copper, stainless steel, and polyethylene naphthalate. These films exhibited enhanced structural stability, environmental stability, and corrosion resistance. The free-standing F-MXene films demonstrated high flexibility, withstanding up to 10 000 bending cycles, and structural stability with a tensile strength of 35 MPa. Notably, the EMI SE of the hydrophobic F-MXene films surpassed that of previously reported hydrophobic MXene films and MXene composites, achieving approximately 52–77 dB at thicknesses of 5–40 μm, compared to 70 dB at 60 μm for prior designs.[23] In an accelerated oxidation test at 80% relative humidity (RH) and 100°C for 49 days, the hydrophobic F-MXene films retained approximately 93% of their initial electrical resistance, whereas pristine MXene films exhibited a 49% decline in pristine MXene films. Additionally, the free-standing F-MXene films demonstrated excellent water resistance, maintaining conductivity even under direct water exposure, unlike pristine MXene films, which degraded immediately upon contact with water. Further testing in a 3.5 wt% NaCl aqueous solution (simulating seawater conditions) under a continuous 1 V current for 7 days confirmed that F-MXene films maintained their current more effectively than commercial Al foil. Finally, F-MXene films proved adaptable to various scalable application methods, including spray coating, paint brushing, and blade coating on both curved and flat surfaces. They exhibited superior adhesion compared to pristine MXene films, further demonstrating their potential for real-world EMI shielding applications.

2 | RESULTS AND DISCUSSION

2.1 | Hydrophobicity of MXene via alkyl amine functionalization

Pristine MXene is intrinsically hydrophilic and disperses easily in water due to its highly negative zeta potential, attributed to surface terminations such as –O and –OH.[4] However, dispersing MXene in nonpolar solvents requires increasing the inter-flake spacing to counteract '*like dissolves like*' effects, primarily driven by London dispersion forces and three-dimensional steric

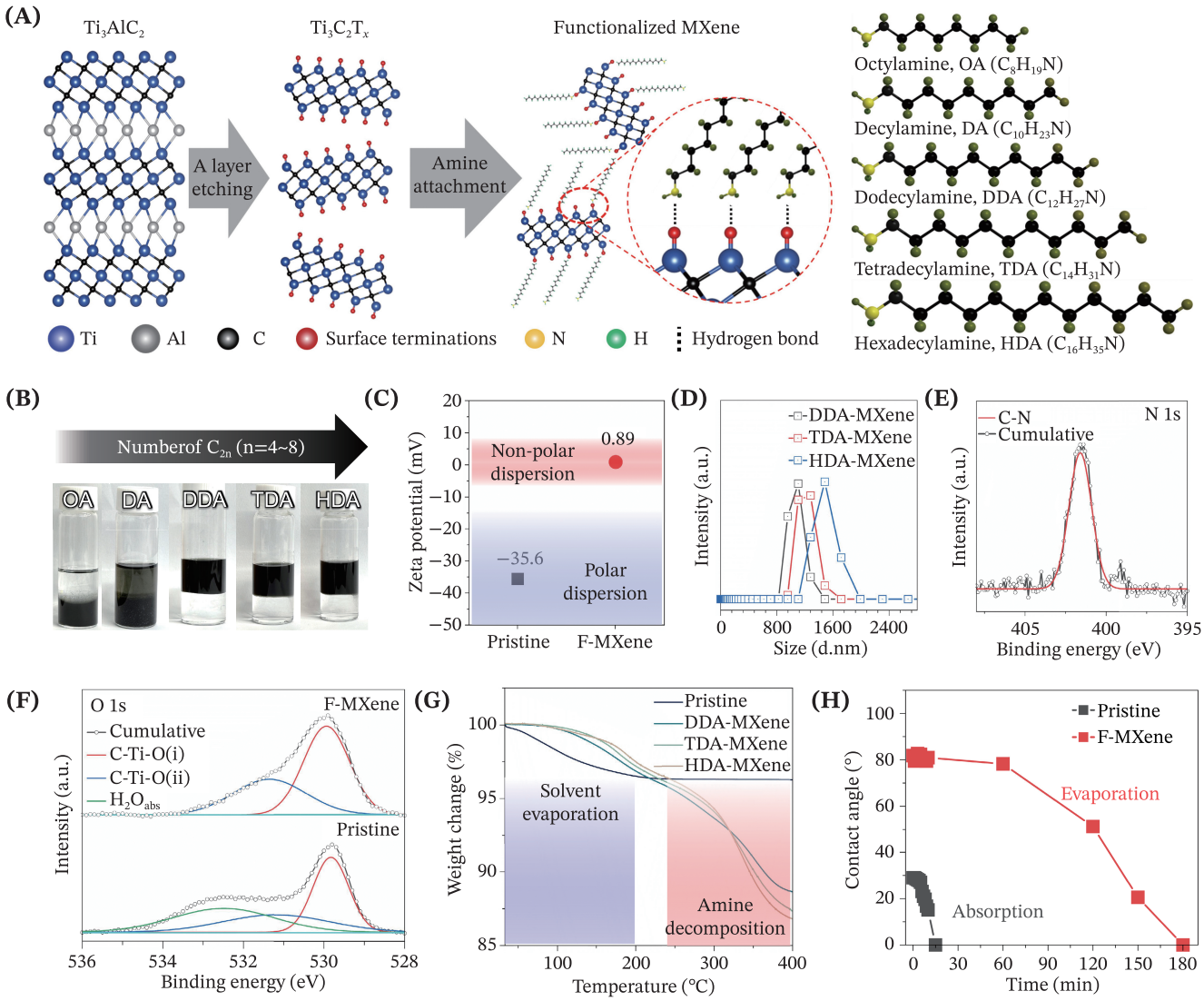

FIGURE 1 Characterizations of hydrophobic 2D F-MXene. (A) Schematic illustration of synthesis and functionalization of 2D MXene and alkyl amines. (B) Photograph image after functionalized process. (C) Zeta potential comparison of MXene and F-MXene. (D) Size distribution of each sample obtained by DLS analysis. (E) XPS analysis of N *1s* of F-MXene. (F) XPS analysis of O *1s* of MXene (bottom) and F-MXene (top). (G) TGA analysis of MXene and F-MXene with different alkyl amines. (H) Changes in water contact angle of MXene and F-MXene with time.

stabilization.[37,38] Figure 1A illustrates the synthesis of MXene, followed by alkyl amine functionalization via hydrogen bonding to increase the inter-flake spacing. X-ray diffraction (XRD) and scanning electron microscopy (SEM) analyses of the Ti_3AlC_2 MAX phase and $Ti_3C_2T_x$ (MXene), with an average flake size of 9.1 μm, confirm the high quality of the MXene employed in this study (Figures S1 and S2). To achieve stable MXene dispersion in nonpolar solvents, the optimal alkylamine chain length was systematically investigated by increasing the chain length in two-carbon increments from octylamine (OA) to hexadecylamine (HDA). While OA and decylamine (DA) provided insufficient inter-flake spacing for stable dispersion, dodecylamine (DDA), tetradecylamine (TDA), and HDA improved flake separation (Figure 1B). However, DDA-functionalized MXene lost its dispersion stability and was sedimented within 3 days, whereas HDA-functionalized MXene remained stable. Consequently, HDA was selected for all subsequent F-MXene samples (Figure S3).

The colloidal stability of F-MXene was confirmed through surface zeta potential measurements and the Tyndall effect (Figures 1C and S4). The near-zero zeta potential of F-MXene indicates that alkyl amine functionalization effectively neutralized the surface dipole of pristine MXene, which originally had a zeta potential of −35.6 mV. Dynamic light scattering (DLS) analysis revealed an increase in hydrodynamic size, with

peak intensities at 1106, 1281, and 1484 nm for DDA-, TDA-, and HDA-functionalized MXenes, respectively, confirming successful alkyl amine attachment (Figure 1D). Atomic force microscopy (AFM) height profiles revealed an increase in flake thickness from 2 to 4 nm, attributed to alkyl amines on both sides of the MXene flakes (Figure S5). Transmission electron microscopy (TEM) images showed that the F-MXene flakes retained their morphology, with clean surfaces, preserving their intrinsic hexagonal structure (Figure S6). Energy-dispersive X*l*-ray spectroscopy (EDS) mapping confirmed the presence of Ti from F-MXene and N from the alkyl amines, validating successful functionalization (Figure S7).

Freestanding F-MXene films were fabricated via vacuum filtration to characterize their physical properties. Cross-sectional SEM and corresponding EDS mapping of the F-MXene films confirmed the homogeneous distribution of Ti, C, and N atoms throughout each alkyl amine-functionalized MXene film (Figure S8). The Raman spectra revealed that the characteristic vibrational modes of MXene at 206, 384, and 723 cm^{-1} remained unchanged in F-MXene, whereas the mode at 590 cm^{-1} shifted to 550 cm^{-1}, suggesting the influence of amine attachment on the Ti surface (Figure S9).[39] Furthermore, the peak at 291.3 cm^{-1}, associated with –OH groups, exhibited a slight red shift to 288.7 cm^{-1} and diminished after functionalization, indicating hydrogen bonding between the amine groups and surface terminations of MXene. Figure 1E presents the X-ray photoelectron spectroscopy (XPS) analysis of the N *1s* region of F-MXene. The presence of C–N bonds rather than Ti–N bonds suggests that alkyl amine is physically attached to the MXene surface through interactions between MXene surface terminations and $–NH_2$ groups rather than Ti–N bonds.[40] XPS analysis also revealed changes in the (i) C–Ti–O peaks and (ii) the peaks associated with the surface termination of O sites, indicating that amine functionalization affects surface titanium, consistent with the Raman data (Figure 1F).[41] The absence of an adsorbed H_2O signal for F-MXene suggests that amine functionalization effectively induces hydrophobicity. Furthermore, the lack of significant shifts in the Ti *2p* or C *1s* binding energies suggests that the amine functionalization does not involve direct chemical bonding (Figure S10). Thermogravimetric analysis (TGA) revealed that, while pristine MXene exhibited weight loss at approximately 100°C due to water evaporation, F-MXene exhibited weight loss at around 150°C, corresponding to the higher boiling point of chlorobenzene (Figure 1G). A notable weight change above 280°C, corresponding to alkyl amine decomposition, further confirmed that F-MXene retained its hydrophobic properties during heat treatment up to approximately 200°C. Figure S11 shows a substantial increase in the water contact angle of alkyl amine-treated MXene compared to pristine MXene, indicating enhanced hydrophobicity due to alkyl chains extending outward from the MXene flake surface. Time-dependent contact angle measurements revealed that pristine MXene rapidly absorbed water, causing the contact angle to reach 0° within 15 min (Figure 1H). In contrast, F-MXene maintained its contact angle, reaching 0° only after 180 min due to water evaporation rather than absorption, demonstrating excellent hydrophobicity (Figure S12).

2.2 | Environmentally robust F-MXene films with High EMI shielding performance

Figure 2A presents the XRD patterns of the pristine and F-MXene films before and after the heat treatment. The (002) peak of pristine MXene shifted gradually from $2\theta \approx 7.10°$ to 5.06° after alkyl amine functionalization due to intercalation of chains and trapped solvent molecules. Heat treatment at 200°C removed the trapped solvents, shifting the (002) peak of F-MXene back to $2\theta \approx 6.40°$. The *d*-spacings were 10 Å for pristine MXene and 14 Å for F-MXene, indicating a 4 Å reduction after heat treatment (Figures 2B and S13). Since the fully stretched chain length of HDA is nearly 20 Å,[42] the changes in *d*-spacings suggest that the alkyl chains of the alkyl amines shrink after solvent removal due to rotational freedom of the C–C bonds. This shrinkage helps maintain the layered structure of MXene. The graft ratio (r_g) was calculated from the change in *d*-spacing using the following equation[43]:

$$r_g(\text{graft ratio}) = \left(l_{\text{exp}} - l_0\right)/(L - l_0), \tag{1}$$

where $_0$ represents the interlayer spacing of pristine MXene (1.24 nm), and l_{exp} is the experimentally observed interlayer spacing. L denotes the theoretical interlayer spacing, given by:

$$L = l_0\left(1 + r_{\text{w}} \cdot \rho_{\text{MXene}}/\rho_{\text{Alkylamine}}\right), \tag{2}$$

where r_{w} is the weight ratio of alkyl amines to MXene, and represents the mass density (3.7 g cm^{-3} for pristine MXene,[44] 0.806 g cm^{-3} for DDA, 0.993 g cm^{-3} for TDA, and 0.94 g cm^{-3} for HDA). The r_{w} values obtained from TGA analysis were 0.078 for DDA, 0.107 for TDA, and 0.110 for HDA. The experimental interlayer spacings

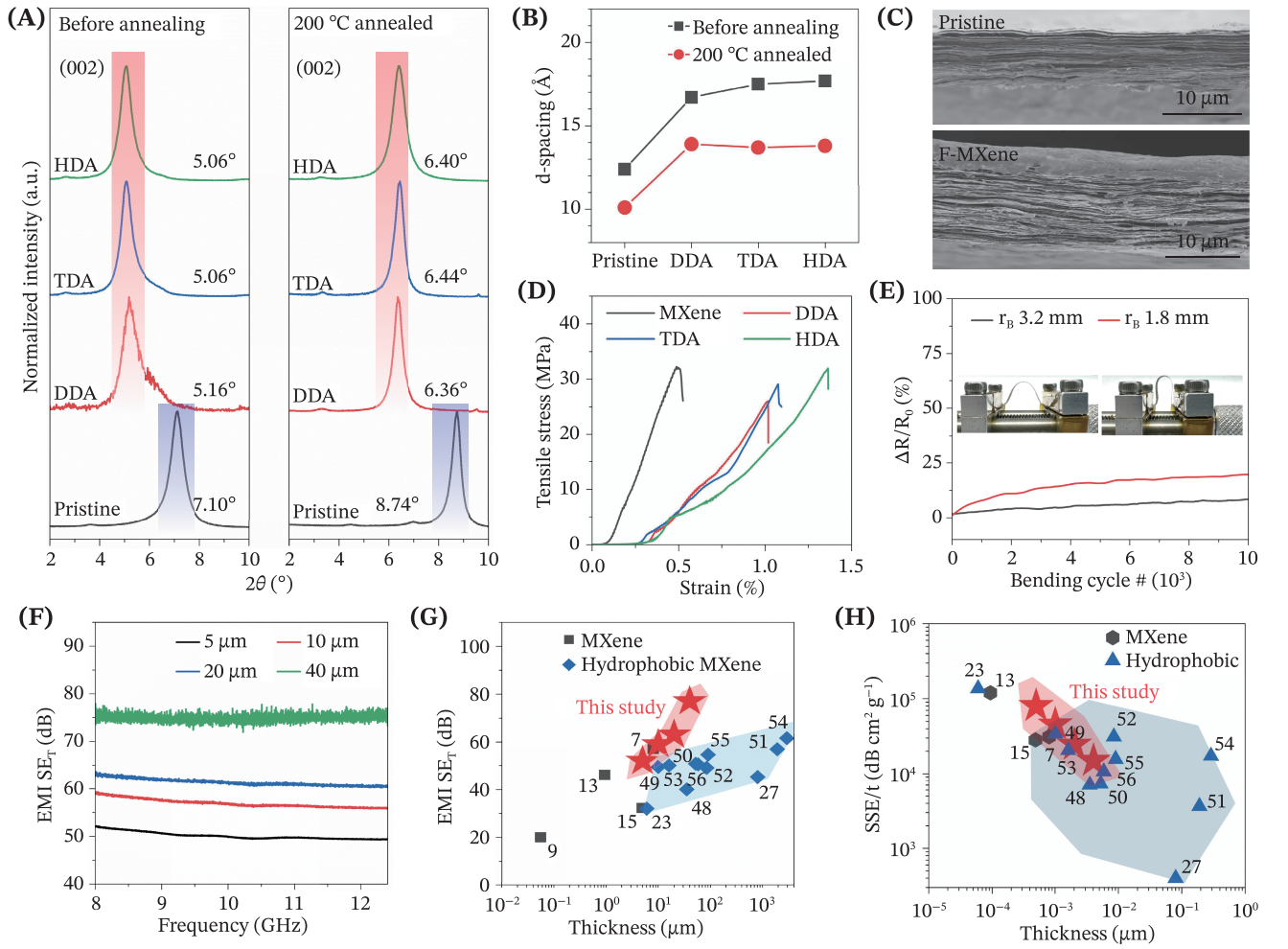

FIGURE 2 Structural robustness of F-MXene with high EMI SE. (A) XRD patterns of MXene and F-MXene with different alkyl amines before and after annealing. (B) *d*-spacing change by different alkyl amines before and after annealing. (C) Cross-sectional SEM images of MXene and F-MXene. (D) Stress–strain curves of MXene and F-MXene decorated by various alkyl amines. (E) Normalized resistance changes vs. bending cycle at bending radii of 3.2 and 1.8 mm. Inset shows photograph images of 3.2- and 1.8-mm-bended F-MXene. (F) EMI shielding effectiveness of F-MXene with different thicknesses. (G) EMI SE_T vs. thickness chart. (H) Absolute EMI shielding effectiveness vs. thickness chart.

(l_{exp}) were 1.67 nm for DDA, 1.75 nm for TDA, and 1.77 nm for HDA, yielding values of 0.98 for DDA_MXene, 1.03 for TDA_MXene, and 0.99 for HDA_MXene. These results suggest that the graft ratios are similar across all functionalized MXenes. This similarity can be attributed to the washing process, which effectively removes excess unattached alkyl amines, leaving behind a consistent amount of grafted material.

Cross-sectional SEM images confirmed that F-MXene maintained an orderly and well-preserved layered structure despite the increase in *d*-spacing (Figure 2C). Mechanical stability was evaluated using stress–strain analysis (Figure 2D). Alkyl amine-functionalized MXenes exhibited tensile strength ranges of 35–40 MPa, while the elongation at fracture increased from 0.5% to 1.3%, indicating reduced inter-flake interactions due to surface-attached alkyl amines (Figure S14). SEM images of fractured F-MXene films after tensile testing revealed a densely packed lamellar structure with curled fracture edges and characteristic "*zigzag*" step-type cracks (Figure S15).[16] Crack propagation initiated as adjacent F-MXene flakes slid against each other. Upon reaching the yield strength, the entangled alkyl chains unraveled, separating adjacent F-MXene flakes and ultimately causing full fracture. This behavior is consistent with the increased tensile strain observed in Figure 2D. The longer the alkylamine chains, the greater the degree and the likelihood of entanglement, leading to enhanced mechanical interlocking within the F-MXene films.[45] A 10 000-cycle bending test on F-MXene, conducted at bending radii of 3.2 and 1.8 mm, demonstrated excellent durability, with resistance increasing by only 8% and 19%, respectively (Figure 2E). These findings highlight the outstanding mechanical flexibility and resilience of

F-MXene, even with alkyl amines positioned between MXene layers.

Prior to the assessment of the EMI shielding performance, the electrical conductivities of the MXene films were analyzed on the basis of the type of alkyl amine, as it directly impacts the EMI SE and depends on both intra- and inter-flake conductivity.[46,47] Alkyl chain attachment resulted in a half-order magnitude decrease in electrical conductivity due to increased interlayer spacing, rather than difference in graft ratios, which remained similar across functionalized MXenes (Figure S16 and Table S1). However, thermal treatment significantly improved electrical conductivities across all samples. For example, DDA-functionalized MXene exhibited an electrical conductivity of 4782 ± 180 S cm^{-1}, the highest reported for hydrophobic MXenes (Table S2).

The EMI SE of F-MXene was evaluated at X-band (8.2–12.4 GHz) across various film thicknesses. Due to its superior electrical conductivity, F-MXene exhibited high EMI SE values of 50.1 ± 1.1, 56.9 ± 1.2, 61.4 ± 1.2, and 75.0 ± 1.3 dB at thicknesses of 5, 10, 20, and 40 μm, respectively (Figure 2F). Notably, at a thickness of 10 μm, F-MXene retained approximately 76% of EMI SE of pristine MXene (Figure S17). Compared with previous studies,[7,9,11,13,23,27,48–56] F-MXene demonstrated exceptional absolute EMI SE despite, its hydrophobic nature, while also maintaining superior electrical conductivity (Figure 2G,H). This was achieved by the strategic placement of alkyl amines between MXene layers, reducing the number of flakes needed for the same thickness, resulting in lower overall density. This moderate trade-off in conductivity significantly improves environmental robustness and mechanical stability while maintaining EMI shielding performance well above commercial standards.

To understand the high EMI SE of F-MXene, its shielding mechanism was investigated (Figure S18). More than 90% of incident EM waves were reflected, while the residual EM waves were absorbed within the film, as indicated by extremely low T values ($T < 0.001$). SE can be calculated using the following coefficients (Figure S19). The reflection SE (SE_R) of the F-MXene films remained constant at approximately 20 dB irrespective of the film thickness. Conversely, the absorption SE (SE_A) increased progressively with thickness, contributing significantly to the total SE (SE_T). These findings indicate that the EMI shielding performance of F-MXene is predominantly driven by the SE_A, consistent with previous reports.[6]

Figure 3A shows the oxidation stability of free-standing films tested at 80% RH and 100°C. Pristine MXene exhibited a resistance increase of $51\% \pm 5\%$ after 49 days, whereas F-MXene showed only a minor increase of $7\% \pm 2\%$, indicating a significantly improved oxidation stability under humid conditions. SEM images revealed that the surface of pristine MXene became contaminated and partially cracked after oxidation, while F-MXene remained unchanged (Figure S20). XPS analysis further confirmed this, with a pronounced increase in the TiO_2 peak for pristine MXene after 49 days (Figure 3B), whereas F-MXene exhibited minimal change (Figure 3C). The exposed alkyl chains on the MXene surface, being non-polar due to the negligible electronegativity difference between carbon and hydrogen atoms, transformed its hydrophilic nature to hydrophobicity. This hydrophobic barrier effectively prevented water molecules from accessing the MXene surface, which is the primary cause of oxidation.[57] Additional confirmation of enhanced oxidation stability was obtained by comparing F-MXene in a non-polar solvent with MXene in water—both stirred at 1000 rpm and 80°C—and monitoring oxidation via ultraviolet–visible (UV–vis) spectroscopy (Figure S21). For pristine MXene, the peak near 780 nm disappeared within 1 day, leaving only the TiO_2 peak at 350 nm, whereas F-MXene retained its characteristic peak for over 35 days, further confirming its superior oxidation resistance. This stability extends the shelf life of F-MXene, reduces storage costs, and minimizes material waste due to oxidation, thereby significantly contributing to cost reduction for industrial use.

Building on its environmental stability, verifying the durability of F-MXene films in water is crucial to assessing their resilience under various conditions, including physically and chemically harsh environments. Pristine MXene films dissolved completely within 60 s of ultrasonication in water, whereas F-MXene retained its structure even after 30 min (Figure S22), demonstrating its resistance to water penetration and structural integrity under external stress. To further confirm the stability of F-MXene in aquatic environments, current values were monitored over time while submerged in water. As shown in Figure 3D, the current in pristine MXene rapidly decreases upon exposure to water, whereas F-MXene maintains a stable current. This finding was reinforced by the electrode setup experiment, where pristine MXene caused the light bulb to turn off in the water, while F-MXene kept it illuminated (Figure 3E).

Beyond its resistance to pure water, F-MXene demonstrated remarkable stability in highly corrosive environments, such as seawater. Figure 3F presents its stability in a 3.5 wt% NaCl solution, simulating seawater conditions. For commercial metals such as Al foil, the current dropped sharply within 24 h, retaining only 0.04% of its initial value after 7 days. In contrast, F-MXene maintained a stable current under these conditions,

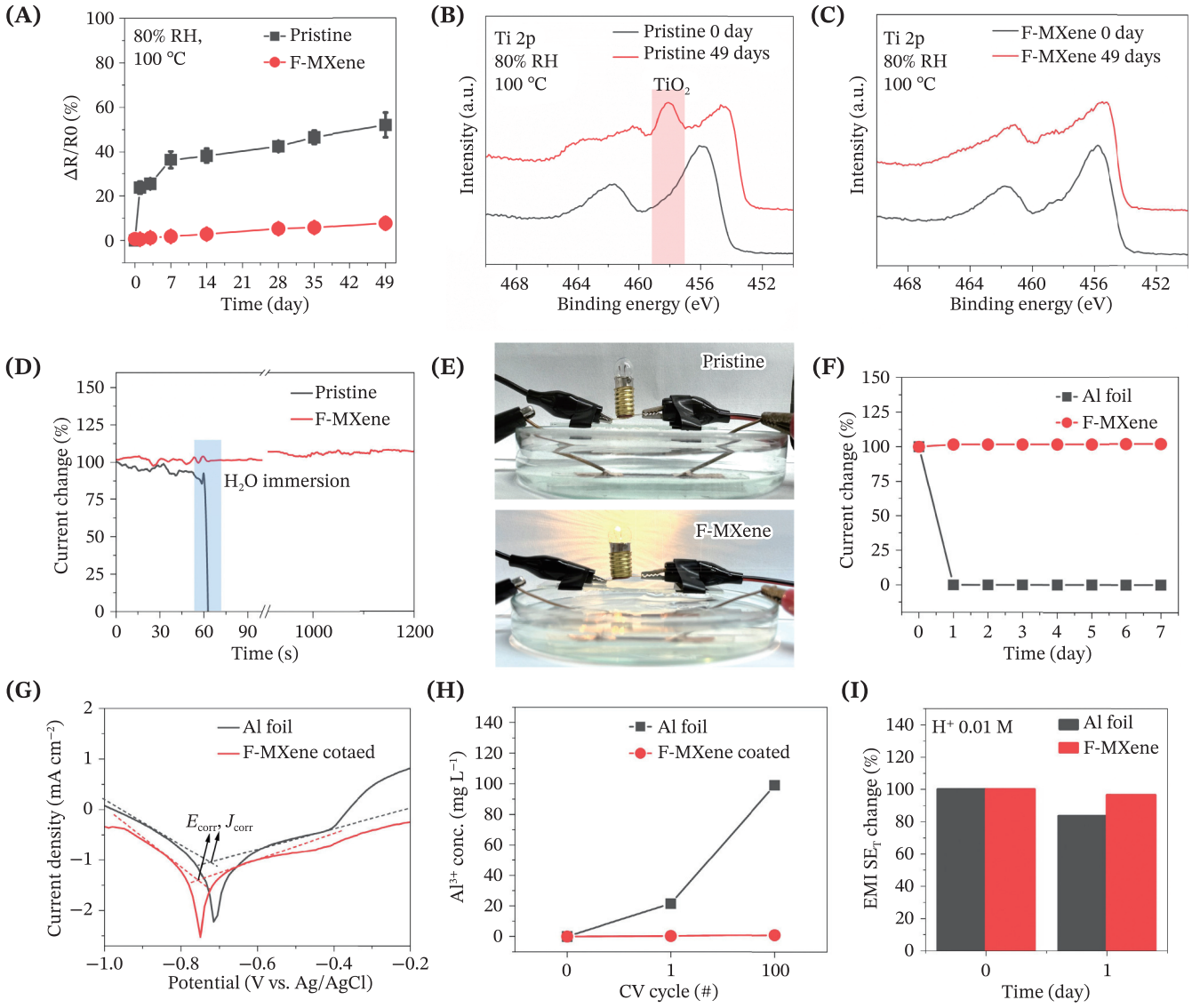

FIGURE 3 Environmentally stable F-MXene. (A) Resistance changes during oxidation test under 80% RH and 100°C. (B, C) XPS analysis of Ti *2p* of MXene and F-MXene after oxidation test. (D) Current value change after water immersion. (E) Photograph images of the light bulb working status after pouring water. (F) Current value change of Al foil and F-MXene under seawater environment. (G) Polarization curves in the electrolyte with or without F-MXene passivation. (H) Al ion concentration before and after CV test. (I) EMI SE comparison of Al and F-MXene by storing in acidic condition.

highlighting its enhanced durability in seawater and corrosive environments. After 1 day of seawater exposure, the current in the Al foil declined and plateaued, indicating corrosion. Significant surface corrosion was also visible, as confirmed by an increased oxygen signal in the EDS analysis, whereas the surface of F-MXene remained unchanged (Figures S23 and S24).

The potential of F-MXene as an anticorrosion barrier was further evaluated. Figure 3G presents the polarization curves of the Al foils with and without an F-MXene coating. The corrosion potential (E_{corr}) of F-MXene-coated Al foil shifted to −0.75 V (slightly more negative than bare Al foil), with a higher corrosion current density (J_{corr}) of −1.43 mA cm^{-2} compared to −1.05 mA cm^{-2} for untreated Al foil. To further validate its anticorrosion capability, the Al ion concentration in the electrolyte was measured using inductively coupled plasma optical emission spectrometry (ICP-OES) (Figure 3H). For bare Al, the Al-ion concentration rose significantly from 0.006 to 99.0 mg L^{-1} after 100 cyclic voltammetry (CV) cycles. In contrast, the F-MXene-coated Al foil exhibited only a minimal increase from 0.003 to 1.05 mg L^{-1}, demonstrating its superior anticorrosion ability. These results established F-MXene not only as a robust film material but also as an effective passivation layer for protecting existing metals from corrosion.

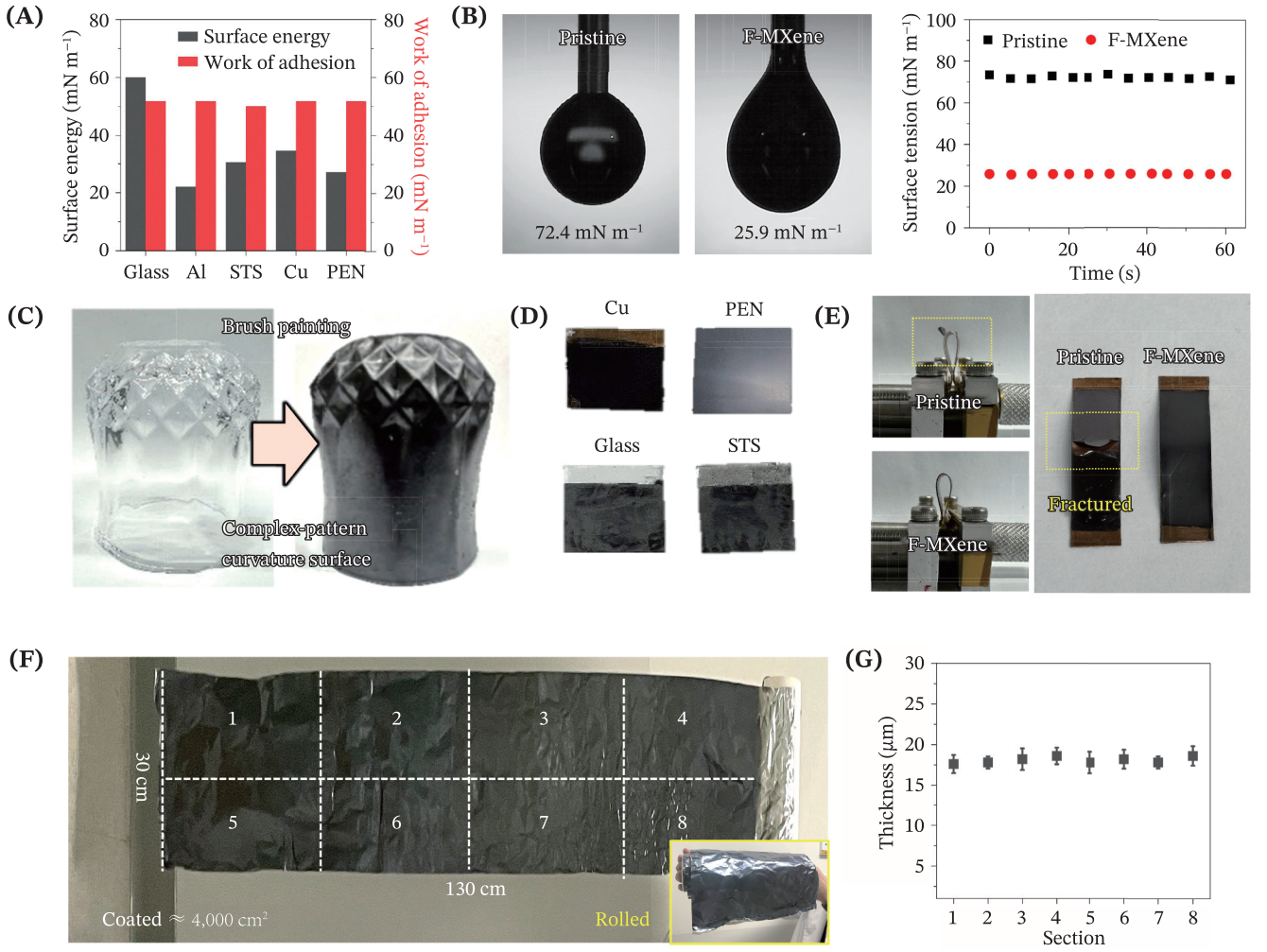

FIGURE 4 Large-scale integration with versatile coating process. (A) Surface energy of different substrates and work of adhesion of F-MXene against different substrates. (B) Surface tension measurement of MXene and F-MXene. Paint brushing of F-MXene ink on (C) complex patterned curvature surface and (D) different substrates. (E) Photograph images of bending MXene- and F-MXene-coated Cu. (F) Photograph images of spray-coated F-MXene on Al foil with divided section and after rolling using Al foil roll (inset). (G) Thickness uniformity of spray-coated Al foil.

2.3 | Large-scale integration through versatile coating

For industrial applications, verifying whether F-MXenes can be processed over large areas using various techniques is necessary. This requires assessing the surface tension of the solution and the surface energy of the substrate for compatibility. Figure 4A presents the surface energies of different substrates calculated using the Owens, Wendt, Rabel, and Kaelble (OWRK) theory and determined through contact angle measurements using water and diiodomethane. The work of adhesion was calculated using the DuPre equation.

$$W_{SL} = \gamma_{SV+} + \gamma_{LV} - \gamma_{SL} = \gamma_{LV}(1 + \cos\theta), \quad (3)$$

where is the work of adhesion for the solid–liquid interface, is the solid–vapor interfacial energy, is the liquid–vapor interfacial energy, and is the solid–liquid interfacial energy. The measured was approximately 51.8 mN m^{-1} for each substrate, indicating strong adhesion.[36] The measured surface tension of pristine MXene in water was 72.4 mN m^{-1}, whereas F-MXene in chlorobenzene exhibited a much lower surface tension of 25.9 mN m^{-1} (Figure 4B). This low surface tension allows F-MXene to be applied directly without additional surface treatment, unlike pristine MXene, which requires UV-ozone or O_2 plasma treatment to increase substrate surface energy for effective processing.[58] The elimination of the pretreatment process to control surface energy can significantly reduce costs, enhancing the feasibility of F-MXene for industrial use.

The low surface tension of F-MXene also enhances wettability across various substrates, confirming its suitability for large-area coating applications (Figure S25). It can be applied using a brush on flat substrates, such as Cu, glass, and stainless steel (STS), as well as on complex-patterned surfaces (Figure 4C,D). When coated on Cu and subjected to bending, pristine MXene began to detach at a bending radius of approximately 4 mm and fully separated at 1.2 mm (Figure 4E). In contrast, F-MXene maintained its structural integrity with no detachment, even at a bending radius of 1.2 mm, indicating its superior coating ability and adhesive properties. As shown in Figure 4F, scalable spray coating is employed to Al foil with a length and width of 130 and 30 cm, respectively. The F-MXene-coated Al foil remained intact without any detachment, even after rolling (inset of Figure 4F). The coated foil was segmented into eight sections to assess uniformity, with the coating evenly distributed across all sections and an average thickness of 18.07 ± 1.08 μm (Figure 4G). Furthermore, the cross-sectional SEM image (Figure S26) revealed that the F-MXene flakes were well aligned and exhibited strong adhesion to the Al foil. Additionally, blade coating was successfully applied over a large area (100 cm^2) on a polyethylene naphthalate (PEN) substrate, with no detachment even after rolling (Figure S27). These results demonstrate not only the feasibility of large-area processing using various methods but also the industrial potential of F-MXene as a durable and highly adhesive sustainable material for diverse substrates.

3 | CONCLUSION

In summary, we developed oxidation- and water-resistant titanium carbide MXenes through alkyl amine-based surface functionalization. This functionalization enabled the dispersion of MXenes in nonpolar solvents via steric stabilization, with the minimum required alkyl chain length experimentally determined. The proposed F-MXenes maintained their high performance and oxidative stability after a single, efficient surface-functionalization step, making them compatible with large-area processing. The optimized F-MXenes exhibited exceptionally high flexibility and structural stability, achieving the highest electrical conductivity among reported hydrophobic MXenes and their composites. This superior conductivity led to enhanced EMI shielding efficiency at reduced thicknesses. Unlike traditional covalent bonding approaches, which often require high temperatures and prolonged heat treatments, the physical bonding approach used in this study enables rapid and straightforward surface functionalization while minimizing damage to MXene. This approach preserves its high electrical conductivity and EMI shielding properties. Furthermore, F-MXene ink can be applied to various metal, plastic, and glass substrates with complex patterns. The highly adhesive F-MXene coating exhibited strong environmental stability under seawater conditions, reinforcing its potential for industrial applications as an effective anticorrosion and passivation coating. Our work bridges the gap between fundamental innovation and practical application by leveraging delaminated 2D MXenes, a mild and scalable functionalization strategy, and industrially relevant film fabrication techniques, thereby enabling a high-performance, large-scale EMI shielding solution that distinguishes our approach from existing methodologies.

4 | EXPERIMENTAL SECTION

4.1 | Ti_3AlC_2 synthesis

TiC (Thermo Fisher Scientific, 99.5%, 2 μm), Ti (Thermo Fisher Scientific, 99.5%, 325 mesh), and Al (Thermo Fisher Scientific, 99.5%, 325 mesh) powders were ball-milled with a molar ratio of 2:1:1.05 for 20 h. A 250 mL flat-bottom high-density polypropylene (HDPE) tube with a zirconia ball size of 3 mm was used for ball milling. The HDPE tube was filled with powder and balls at a weight ratio of 1:10. Ball-milled powder was then placed into an alumina crucible, sintered at a rate of 5°C min^{-1} to 1450°C, and held for 2 h under an Ar flow of 0.5 NL min^{-1}. The sintered Ti_3AlC_2 was ground using an agate mortar and pestle and sieved through a 325 mesh for further use.

4.2 | $Ti_3C_2T_x$ synthesis

1 g of Ti_3AlC_2 was poured into a mixed etchant consisting of 2 mL of hydrofluoric acid (Alfa Aesar, 48%–51%), 8 mL of DI water, and 10 mL of hydrochloric acid (Sigma Aldrich, 36.5%–38.0%) and was continuously stirred for 24 h at 35°C for etching the Al layer. The etched multilayer MXene was then washed with DI water via centrifugation at 3500 rcf for 5 min until the pH of the supernatant reached approximately 6 (typically 3–4 times), using a 250 mL conical polypropylene (PP) centrifuge tube. Subsequently, 1 g of lithium chloride (Sigma-Aldrich, ≥99%) was dissolved in 10 mL of DI water in a 50 mL conical PP tube and mixed at 3200 rpm using a vortex mixer with multilayer MXene for 1 h. After 1 h, the Li-intercalated multilayer MXene was washed via centrifugation at 3500 rcf for 5 min until self-

delamination occurred (typically 3–4 times). When self-delamination occurred, the supernatant and sediment were mixed and distributed equally into four 250 mL conical centrifuge tubes. The supernatant was collected by repeated centrifugation for 5 min at 3500 rcf, and the corresponding process was repeated until the dark color of the supernatant became faded. The dark supernatant was collected and concentrated at 12 000 rcf for 30 min.

4.3 | Size selection of $Ti_3C_2T_x$

The prepared solution was placed in a 250 mL conical centrifuge tube and centrifuged at 2500 rcf for 5 min. The supernatant was carefully separated, centrifuged at 12 000 rcf for 10 min, and stored for surface functionalization. The average lateral size of the MXene flakes dispersed in the supernatant was measured using SEM.

4.4 | Surface functionalization

OA (TCI, n-octylamine), DA (TCI, 1-Aminodecane), DDA (Sigma-Aldrich, dodecylamine), TDA (TCI, Tetradecylamine), and HDA (Acros Organics, 1-Hexadecylamine) were added to the prepared MXene solution and thoroughly mixed using a vortex mixer. The mixture was then centrifuged at 3500 rcf for 5 min, and the excess alkylamine present in the sediment was removed by washing with ethanol (Daejung, Ethyl alcohol) and chlorobenzene (Daejung, Monochlorobenzene) through additional centrifugation. Finally, the washed sediment was dispersed in chlorobenzene for further use.

4.5 | Characterization

XRD patterns were recorded using a high-power XRD instrument (Rigaku, D/MAX2500V/PC) with Cu Kα radiation (40 kV, 200 mA) with a scan step of 0.02°. The morphologies and cross sections of the samples were studied using Cold SEM (Hitachi, S-4800). TEM images and SAED patterns were acquired using a TEM instrument (JEOL, JEM-2100). AFM images were acquired using a Bruker Dimension AFM instrument operating in tapping mode. XPS was performed using a Thermo Fisher K-Alpha instrument. DLS (Zetasizer, Malvern, Nano ZS) analysis was performed to obtain the size distribution. The mechanical properties were measured using freestanding films cut into strips (10 mm × 30 mm) for tensile testing. Three strips per sample were tested using an LS1 material testing machine (Lloyd) with a 10-N load cell. The strips were then pulled at a rate of 0.01 mm s^{-1}. The specimens were held at a grip distance of approximately 10 mm. The tensile strength was calculated using the maximum stress and cross-sectional area of the strips before failure. For the bending test, the freestanding film was cut into 5 mm × 30 mm strips and mounted onto grips, which were repeatedly bent in one direction while establishing an electrical connection. Electrical conductivity was calculated using the sheet resistance measured by a 4 point-probe (AIT, CMT2000N), and the average thickness was measured using SEM cross-sectional images. Thermal stability data were collected using thermogravimetric analyses (TGA, TA, and Q500). Contact angle and surface energy of substrates was measured with a goniometer (KRÜSS GmbH, DSA100) and surface tension of fabricated inks was measured with Smartdrop (Femtofab, SDL200TEZD). The surface was calculated according to the OWRK theory. The corrosion test was conducted using an electrochemical analyzer (Iviumstat2.h, Ivium Technologies), and the electrochemical cell was composed of three electrodes: a 1 × 1 cm^2 specimen as the working electrode, a Pt wire as the counter electrode, and an Ag/AgCl electrode as the reference electrode. Potentiodynamic polarizations were performed in a 3.5 wt% NaCl solution at room temperature. The potential range was from −0.8 to 0.2 V, and the scan rate was 1 mV s^{-1}. CV sweeps were performed under the same conditions at a scan rate of 100 mV s^{-1}. The current level was measured at 1 V using an electrochemical analyzer after connecting the specimen to the Cu wire. The S parameter and EM parameters of samples were measured using a two-port vector network analyzer (VNA, model N5247A, Agilent), combined with a millimeter head controller (N5261A, Agilent), a frequency extender (N5260-60003, Agilent), and rectangular waveguides covering the X (8.2–12.4 GHz) frequency bands. Standard calibration was performed using the Thru, Reflect, and Line (TRL) method.

Reflection (R), absorption (A), and transmission (T) coefficients were determined from the measured S-parameters using the following equations:

$$R = |S_{11}|^2 = |S_{22}|^2, \tag{4}$$

$$T = |S_{21}|^2 = |S_{12}|^2, \tag{5}$$

$$A = 1 - R - T, \tag{6}$$

The total EMI shielding effectiveness (SE_T), reflection loss (SE_R), absorption loss (SE_A), and multiple reflection loss (SE_{MR}) were described as:

$$SE_T = SE_R + SE_A + SE_{MR}, \tag{7}$$

$$SE_T = 10\log\left(\frac{1}{\mathrm{T}}\right) = 10\log\left(\frac{1}{|S_{21}|^2}\right), \tag{8}$$

$$SE_R = 10\log\left(\frac{1}{1-\mathrm{R}}\right) = 10\log\left(\frac{1}{1-|S_{11}|^2}\right), \tag{9}$$

$$SE_A = 10\log\left(\frac{1-\mathrm{R}}{\mathrm{T}}\right) = 10\log\left(\frac{1-|S_{11}|^2}{|S_{21}|^2}\right), \tag{10}$$

When the total shielding effectiveness (SE_T) exceeds 15 dB, SE_{MR} is typically neglected, allowing SE_T to be expressed as follows:

$$SE_T = SE_R + SE_A, \tag{11}$$

ACKNOWLEDGMENTS

Young Ho Jin and Ju-Hyoung Han contributed equally to this work. This research was supported by the National Research Foundation (NRF) of Korea, funded by the Ministry of Science and ICT (MSIT) (Grant Nos. RS-2024-00408180, RS-2024-00344270), and by the Korea Institute of Energy Technology Evaluation and Planning (KETEP), funded by the Ministry of Trade, Industry & Energy (MOTIE) (Grant No. RS-2024-00398425).

CONFLICT OF INTEREST STATEMENT

The authors declare no conflict of interest.

ORCID

Sung Hyun Park https://orcid.org/0000-0002-0784-8026
Soon-Yong Kwon https://orcid.org/0000-0002-2432-0418

REFERENCES

1. VahidMohammadi A, Rosen J, Gogotsi Y. The world of two-dimensional carbides and nitrides (MXenes). *Science*. 2021; 372(6547):eabf1581.
2. Zhou H, Han SJ, Lee HD, et al. Overcoming the limitations of MXene electrodes for solution-processed optoelectronic devices. *Adv Mater*. 2022;34(41):2206377.
3. Seok S-H, Sim Y, Han J-H, et al. Synthesis and processing of two-dimensional nitride MXenes for electrocatalysis and energy storage. *Cell Rep Phys Sci*. 2023;4(9):101582.
4. Han J-H, Seok S-H, Jin YH, et al. Robust 2D layered MXene matrix–boron carbide hybrid films for neutron radiation shielding. *Nat Commun*. 2023;14(1):6957.
5. Liu C, Feng Z, Yin T, et al. Multi-interface engineering of MXenes for self-powered wearable devices. *Adv Mater*. 2024; 36(42):2403791.
6. Iqbal A, Shahzad F, Hantanasirisakul K, et al. Anomalous absorption of electromagnetic waves by 2D transition metal carbonitride Ti_3CNT_x (MXene). *Science*. 2020;369(6502):446-450.
7. Shahzad F, Alhabeb M, Hatter CB, et al. Electromagnetic interference shielding with 2D transition metal carbides (MXenes). *Science*. 2016;353(6304):1137-1140.
8. Downes M, Shuck CE, McBride B, Busa J, Gogotsi Y. Comprehensive synthesis of $Ti_3C_2T_x$ from MAX phase to MXene. *Nat Protoc*. 2024;19(6):1807-1834.
9. Yun T, Kim H, Iqbal A, et al. Electromagnetic shielding of monolayer MXene assemblies. *Adv Mater*. 2020;32(9): 1906769.
10. Du Y, Yan Z, You W, et al. Balancing MXene surface termination and interlayer spacing enables superior microwave absorption. *Adv Funct Mater*. 2023;33(34):2301449.
11. Wang X-Y, Liao S-Y, Wan Y-J, et al. Electromagnetic interference shielding materials: recent progress, structure design, and future perspective. *J Mater Chem C*. 2022;10(1):44-72.
12. Zhao MQ, Trainor N, Ren CE, Torelli M, Anasori B, Gogotsi Y. Scalable manufacturing of large and flexible sheets of MXene/graphene heterostructures. *Adv Mater Technol*. 2019; 4(5):1800639.
13. Zhang J, Kong N, Uzun S, et al. Scalable manufacturing of free-standing, strong $Ti_3C_2T_x$ MXene films with outstanding conductivity. *Adv Mater*. 2020;32(23):2001093.
14. Zhou T, Cao C, Yuan S, et al. Interlocking-governed ultrastrong and highly conductive MXene fibers through fluidics-assisted thermal drawing. *Adv Mater*. 2023;35(51):2305807.
15. Seok S-H, Choo S, Kwak J, et al. Synthesis of high quality 2D carbide MXene flakes using a highly purified MAX precursor for ink applications. *Nanoscale Adv*. 2021;3(2):517-527.
16. Li W, Zhou T, Zhang Z, et al. Ultrastrong MXene film induced by sequential bridging with liquid metal. *Science*. 2024; 385(6704):62-68.
17. Soomro RA, Zhang P, Fan B, Wei Y, Xu B. Progression in the oxidation stability of MXenes. *Nano Micro Lett*. 2023;15(1):108.
18. Huang S, Mochalin VN. Hydrolysis of 2D transition-metal carbides (MXenes) in colloidal solutions. *Inorg Chem*. 2019;58(3): 1958-1966.
19. Chen H, Wen Y, Qi Y, Zhao Q, Qu L, Li C. Pristine titanium carbide MXene films with environmentally stable conductivity and superior mechanical strength. *Adv Funct Mater*. 2020; 30(5):1906996.
20. Cao F, Zhang Y, Wang H, et al. Recent advances in oxidation stable chemistry of 2D MXenes. *Adv Mater*. 2022;34(13): 2107554.
21. Zhao L, Bi L, Hu J, et al. Universal salt-assisted assembly of MXene from suspension on polymer substrates. *Nat Commun*. 2024;15(1):10027.
22. Yan J, Zhou T, Yang X, et al. Strong and tough MXene bridging-induced conductive nacre. *Angew Chem Int Ed*. 2024; 63(30):e202405228.
23. Liu J, Zhang HB, Sun R, et al. Hydrophobic, flexible, and lightweight MXene foams for high-performance

electromagnetic-interference shielding. *Adv Mater*. 2017; 29(38):1702367.
24. Natu V, Hart JL, Sokol M, Chiang H, Taheri ML, Barsoum MW. Edge capping of 2D-MXene sheets with polyanionic salts to mitigate oxidation in aqueous colloidal suspensions. *Angew Chem*. 2019;131(36):12785-12790.
25. Zhao X, Vashisth A, Prehn E, et al. Antioxidants unlock shelf-stable $Ti_3C_2T_x$ (MXene) nanosheet dispersions. *Matter*. 2019; 1(2):513-526.
26. Liu Y, Li E, Yan Y, et al. A one-structure-layer PDMS/Mxenes based stretchable triboelectric nanogenerator for simultaneously harvesting mechanical and light energy. *Nano Energy*. 2021;86:106118.
27. Raagulan K, Braveenth R, Kim BM, et al. An effective utilization of MXene and its effect on electromagnetic interference shielding: flexible, free-standing and thermally conductive composite from MXene–PAT–poly (p-aminophenol)–polyaniline co-polymer. *RSC Adv*. 2020;10(3):1613-1633.
28. Yan J, Chen M, Tan R, et al. Flexible multifunctional MXene@Ag nanowires/cotton fabric inspired by transport of nutrients by roots for electromagnetic shielding, infrared stealth, joule/solar heating and flame retardancy. *J Mater Chem A*. 2024;12(47):33162-33176.
29. Yan J, Lin C, Jiang S, et al. Fabrication of flexible Co_3Fe_7@Ti_3C_2T_/TiO_2/C@ spacer fabrics for tunable radar-infrared compatible stealth inspired by layered structure of rock. *Chem Eng J*. 2024;499:156409.
30. Zhang Q, Lai H, Fan R, Ji P, Fu X, Li H. High concentration of $Ti_3C_2T_x$ MXene in organic solvent. *ACS Nano*. 2021;15(3):5249-5262.
31. Doo S, Chae A, Kim D, et al. Mechanism and kinetics of oxidation reaction of aqueous $Ti_3C_2T_x$ suspensions at different pHs and temperatures. *ACS Appl Mater Interfaces*. 2021;13(19): 22855-22865.
32. Shin H, Lee H, Seo Y, Jeong W, Han TH. Grafting behavior of amine ligands for surface modification of MXene. *Langmuir*. 2023;39(6):2358-2367.
33. Lee JT, Wyatt BC, Davis GA Jr, et al. Covalent surface modification of $Ti_3C_2T_x$ MXene with chemically active polymeric ligands producing highly conductive and ordered microstructure films. *ACS Nano*. 2021;15(12):19600-19612.
34. Kim D, Ko TY, Kim H, Lee GH, Cho S, Koo CM. Nonpolar organic dispersion of 2D $Ti_3C_2T_x$ MXene flakes via simultaneous interfacial chemical grafting and phase transfer method. *ACS Nano*. 2019;13(12):13818-13828.
35. Zhou C, Wang D, Lagunas F, et al. Hybrid organic–inorganic two-dimensional metal carbode MXenes with amido- and imido-terminated surfaces. *Nat Chem*. 2023;15(12):1722-1729.
36. Chen M, Li L, Deng Z, et al. Two-dimensional janus MXene inks for versatile functional coatings on arbitrary substrates. *ACS Appl Mater Interfaces*. 2023;15(3):4591-4600.
37. Liptrot DJ, Power PP. London dispersion forces in sterically crowded inorganic and organometallic molecules. *Nat Rev Chem*. 2017;1(1):0004.
38. Worthen AJ, Tran V, Cornell KA, Truskett TM, Johnston KP. Steric stabilization of nanoparticles with grafted low molecular weight ligands in highly concentrated brines including divalent ions. *Soft Matter*. 2016;12(7):2025-2039.
39. Sarycheva A, Gogotsi Y. Raman spectroscopy analysis of the structure and surface chemistry of $Ti_3C_2T_x$ MXene. *Chem Mater*. 2020;32(8):3480-3488.
40. Jaeger D, Patscheider J. A complete and self-consistent evaluation of XPS spectra of TiN. *J Electron Spectrosc Relat Phenom*. 2012;185(11):523-534.
41. Natu V, Benchakar M, Canaff C, Habrioux A, Celerier S, Barsoum MW. A critical analysis of the x-ray photoelectron spectra of $Ti_3C_2T_z$ MXenes. *Matter*. 2021;4(4):1224-1251.
42. Wood MH, Welbourn RJ, Charlton T, Zarbakhsh A, Casford M, Clarke SM. Hexadecylamine adsorption at the iron oxide–oil interface. *Langmuir*. 2013;29(45):13735-13742.
43. Yang K, Liang S, Zou L, et al. Intercalating oleylamines in graphite oxide. *Langmuir*. 2012;28(5):2904-2908.
44. Ghidiu M, Lukatskaya MR, Zhao M-Q, Gogotsi Y, Barsoum MW. Conductive two-dimensional titanium carbide 'clay' with high volumetric capacitance. In: *MXenes and Their Composites: Synthesis, Properties and Applications*, edited by M. Alhabeb, CRC Press, 2023, pp. 309–328.
45. Gao Y, Duan L, Guan S, et al. The effect of hydrophobic alkyl chain length on the mechanical properties of latex particle hydrogels. *RSC Adv*. 2017;7(71):44673-44679.
46. Hart JL, Hantanasirisakul K, Lang AC, et al. Control of MXenes' electronic properties through termination and intercalation. *Nat Commun*. 2019;10(1):522.
47. Isari AA, Ghaffarkhah A, Hashemi SA, Wuttke S, Arjmand M. Structural design for EMI shielding: from underlying mechanisms to common pitfalls. *Adv Mater*. 2024;36(24):2310683.
48. Zhou B, Zhang Z, Li Y, et al. Flexible, robust, and multifunctional electromagnetic interference shielding film with alternating cellulose nanofiber and MXene layers. *ACS Appl Mater Interfaces*. 2020;12(4):4895-4905.
49. Liu Z, Wang W, Tan J, et al. Bioinspired ultra-thin polyurethane/MXene nacre-like nanocomposite films with synergistic mechanical properties for electromagnetic interference shielding. *J Mater Chem C*. 2020;8(21):7170-7180.
50. Gao Q, Pan Y, Zheng G, Liu C, Shen C, Liu X. Flexible multilayered MXene/thermoplastic polyurethane films with excellent electromagnetic interference shielding, thermal conductivity, and management performances. *Adv Compos Hybrid Mater*. 2021;4(2):274-285.
51. Lu Z, Jia F, Zhuo L, Ning D, Gao K, Xie F. Micro-porous MXene/aramid nanofibers hybrid aerogel with reversible compression and efficient EMI shielding performance. *Composites Part B*. 2021;217:108853.
52. Aakyiir M, Kingu MAS, Araby S, et al. Stretchable, mechanically resilient, and high electromagnetic shielding polymer/MXene nanocomposites. *J Appl Polym Sci*. 2021; 138(22):50509.
53. Ahmed S, Li B, Luo S, Liao K. Heterogeneous $Ti_3C_2T_x$ MXene-MWCNT@MoS_2 film for enhanced long-term electromagnetic interference shielding in the moisture environment. *ACS Appl Mater Interfaces*. 2023;15(42):49458-49467.
54. Wu S, Chen D, Han W, et al. Ultralight and hydrophobic MXene/chitosan-derived hybrid carbon aerogel with hierarchical pore structure for durable electromagnetic interference shielding and thermal insulation. *Chem Eng J*. 2022;446: 137093.

55. Cheng Y, Li X, Qin Y, et al. Hierarchically porous polyimide/$Ti_3C_2T_x$ film with stable electromagnetic interference shielding after resisting harsh conditions. *Sci Adv*. 2021;7(39):eabj1663.
56. Sha Z, He H, Ma H, et al. All-in-one integrated flexible PE@PET/MXene films for high-performance electromagnetic shields with self-reinforced conductivity and mechanical properties. *Carbon*. 2024;216:118595.
57. Tosuwan P, Leese HS, Chuck CJ. Developing hydrophobic alginate-amine derivatives as a coating for food packaging. *ACS Appl Polym Mater*. 2024;6(17):10669-10677.
58. Jothi Prakash C, Prasanth R. Approaches to design a surface with tunable wettability: a review on surface properties. *J Mater Sci*. 2021;56(1):108-135.

SUPPORTING INFORMATION

Additional supporting information can be found online in the Supporting Information section at the end of this article.

How to cite this article: Jin YH, Han J-H, Park J, et al. Water- and oxidation-resistant MXenes for advanced electromagnetic interference shielding applications. *InfoMat*. 2025;7(9):e70034. doi:10.1002/inf2.70034